Richtmyer-Meshkov Experiments on the Nova Laser at High Compression

Guy Dimonte and Bruce Remington
Lawrence Livermore National Laboratory, Livermore, California 94550
(Received 30 November 1992)

We investigate the shock induced Richtmyer-Meshkov instability at high compression using the Nova laser. The instability and shock characteristics are measured radiographically in planar two-fluid targets with Atwood number <0. The growth of imposed interfacial perturbations $\eta=\eta_0 \sin kx$ agrees with linear theory if the pre- and postshock initial amplitudes are averaged. When $k\eta\sim 2$, the fundamental mode saturates and harmonics emerge producing a slowly developing bubble and spike.

PACS numbers: 52.35.Py, 52.65.+z, 52.70.−m

When a shock passes from one fluid to another with different densities ρ_1 and ρ_2, respectively, perturbations at the interface grow via the Richtmyer-Meshkov (RM) instability [1,2]. For an Atwood number $A=(\rho_2-\rho_1)/(\rho_2+\rho_1)>0$, the predicted growth rate is [1]

$$d\eta/dt = A^* U k \eta_0^* , \quad (1)$$

where $k=2\pi/\lambda$, η, and η_0 are the wave number, and instantaneous and initial amplitudes of the interfacial perturbations, and U is the shock induced velocity of the interface. Asterisks denote postshock values which differ from preshock values because of compression, e.g., $\eta_0^* = \eta_0(1-U/V_1)$, where V_1 is the shock speed in the first fluid. The RM instability causes interfluid mixing similar to the Rayleigh-Taylor (RT) instability [3], but there are important differences because the former is impulsive and involves compression. The RM instability grows at a constant rate and for all $A\neq 0$ whereas the RT instability grows exponentially in time and only for $A>0$ during acceleration. Both instabilities must be controlled in inertial confinement fusion because the resultant mixing contaminates the fuel [4].

The RM instability has been studied extensively, yet fundamental questions remain because experiments disagree with calculations. For $A>0$, Eq. (1) agrees with two-dimensional (2D) simulations [5–7]. For $A<0$, Eq. (1) is invalid, but Meyer and Blewett [5] used simulations to show that Eq. (1) is suitable if η_0^* is replaced with $(\eta_0+\eta_0^*)/2$. In contrast, the growth rates measured in shock tubes [2,7] are much smaller than calculated from theory [1] and simulations [5,6]. This discrepancy is attributed to boundary effects and to the diaphrams separating the gases. To mitigate these problems, experiments were conducted in liquids shocked by high explosives [8], but the interface decelerated in flight which excited the RT instability ($A<0$) and complicated the interpretation.

To resolve this long-standing discrepancy, we investigate the shock induced growth of sinusoidal interfacial perturbations in a planar two-fluid target using the Nova laser. The large compression on Nova provides a stringent test of linear theory because the pre- and postshock parameters differ significantly. The RM instability is isolated by minimizing RT growth by (1) tailoring the Nova drive to maintain a constant interface velocity and (2) using a target with $A<0$. The target is radiographed in flight from two directions: a face-on view for the perturbation growth and a side-on view for the shock characteristics. We find that, contrary to previous experiments, the linear growth rates agree with the Meyer-Blewett prescription for $A<0$. When $\eta\sim\lambda/3$, the fundamental mode saturates and harmonics emerge producing a slowly developing bubble and spike [9].

The experimental configuration is shown in Fig. 1. Eight Nova beams deliver 30 kJ at 0.53 μm into a cylindrical *Hohlraum* to create a uniform soft-x-ray drive which accelerates a target mounted across a hole in the *Hohlraum*. The laser pulse shape is designed to generate a strong shock in the target and to maintain compression and constant velocities for RT stability. The target consists of two solids, an ablator and payload, which become plasmas as a result of x-ray preheat and the shock. The target is radiographed from two directions using high energy x rays generated by irradiating a foil with an independently timed ninth Nova beam of 5 ns duration. The instability amplitude is deduced from the areal density $\rho_2 dz$ which is measured with radiography normal to the interface using 2.6 keV Mo x rays and the 22× Wolter microscope [10]. This technique is checked on

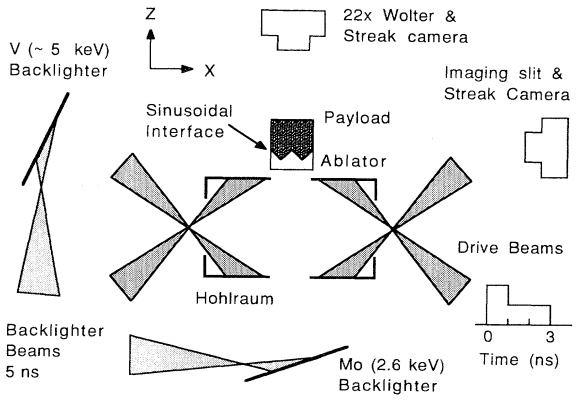

FIG. 1. Experimental configuration.

Nova by radiographing undriven targets with known perturbations. The shock characteristics are measured with transverse radiography using 5–5.5 keV x rays to traverse the target. Since the 22× sensitivity is low above 3 keV, these radiographs are taken with a 1D imaging slit (10 μm×250 μm) coupled to an x-ray streak camera [11]. The slit is oriented parallel to the interface and images in the shock propagation direction with $\delta z \sim 15$ μm resolution FWHM, but integrates along the interface for increased signal. The images are recorded on film, digitized with a photodensitometer, and analyzed on a μVax. Digitized images are converted to exposure units using a film calibration wedge and the natural logarithm is taken to obtain images in optical depth.

Two targets are studied with identical ablators but with different payloads to vary the Atwood number. The ablator is Be because (1) it has a higher density than either payload so that $A < 0$ for RT stability during acceleration and (2) it is transparent to the diagnostic x rays so that the radiographs are insensitive to ablation front instabilities [12]. The payloads are doped to adjust their opacity to diagnostic x rays. A highly unstable target ($A \sim -0.9$) has a foam payload of density $\rho_2 \sim 0.115$ g/cm^3. The foam consists of a CH_2O matrix called AGAR with ~ 2 μm cells and a density of 0.058 g/cm^3. The x-ray dopant is Na_2WO_4 with density 0.057 g/cm^3. A more stable target ($A \sim -0.3$) has a plastic CH payload of density $\rho_2 \sim 1.1$ g/cm^3 with a Br (~ 0.7 at.%) dopant.

Corrugations are imposed at the ablator-payload interface to seed the instability. They are first machined with a numerically controlled diamond turning machine on a copper mold because Be is hard and brittle. The Be is vapor plated onto the Cu mold, lapped flat, cut into disks using electric discharge machining, and removed from the mold with nitric acid. This produces 100 μm thick Be disks which are corrugated on one side and flat on the other. The vapor deposition causes the Be density to be $\sim 90\%$ of bulk density with $\rho_1 \sim 1.7$ g/cm^3. Payloads are then molded to the Be disk to reproduce the corrugations. The AGAR is cast while in solution and then freeze dried into foam. The plastic payload is hot pressed onto the Be disk. The targets are radiographed at each stage to check their purity and opacity.

Figure 2(a) is a transverse radiograph showing the shock characteristics in AGAR. The color scale indicates the optical depth τ for V (5–5.5 keV) x rays. The shock propagates along the z axis, which is referenced to the *Hohlraum* wall at $t = 0$. The *Hohlraum* is expanding as indicated by the dark region at the bottom. The transparent Be ($\tau < 0.4$) is represented by the bright (yellow) region above the *Hohlraum*. The uppermost bright re-

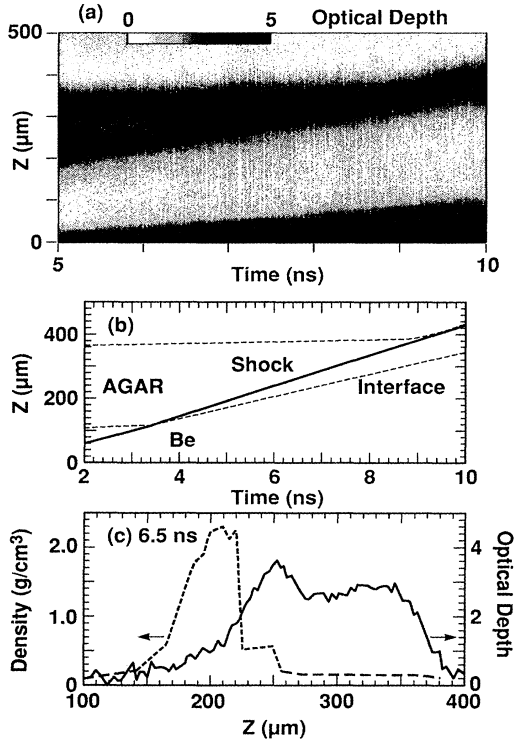

FIG. 2. (a) Transverse radiograph in optical depth of Be/AGAR target showing the shock characteristics. (b) Shock and interface trajectories from 1D LASNEX simulation. (c) Measured optical depth (solid) and calculated density (dashed) profiles at 6.5 ns.

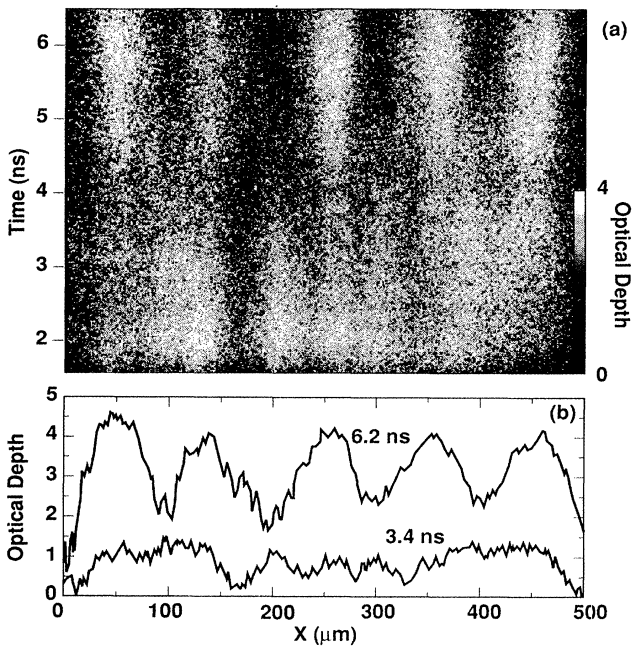

FIG. 3. (a) Face-on radiograph of Be/AGAR target showing instability growth. (b) Optical depth profiles averaged over 0.4 ns. Initial perturbations have $\lambda = 100$ μm, $\eta_0 = 14$ μm.

gion is the empty space behind the AGAR. In between, the uncompressed AGAR is red with $\tau \sim 2$ while the shocked AGAR is more dense and opaque as indicated by the dark strip that is widening in time. The Be/AGAR interface is flat ($\eta_0 = 0$) here for clarity and attains a velocity $U \sim 35$ μm/ns. The shock has a velocity $V_2 \sim 46$ μm/ns in AGAR and reaches the rear surface at 9 ns. Prior to shock breakout, the AGAR expands $\Delta z \sim 20$ μm due to x-ray preheat.

Figures 2(b) and 2(c) show calculations with the radiation hydrodynamics simulation code LASNEX [13]. The measured x-ray drive is applied in the code at the Be ablation surface. The drive is adjusted within the 10% experimental uncertainty so that the shock and interface trajectories in Fig. 2(b) agree with those in Fig. 2(a) and other radiographs taken earlier in time. In the calculation, the incident shock compresses the Be threefold to ~ 5 g/cm^3 and reaches the interface at 3.4 ns with a velocity $V_1 \sim 40$ μm/ns. A shock is reflected from the interface which decompresses the Be to an equilibrium density of $\rho_1^* \sim 2.2$ g/cm^3. The compression and V_1 in Be are not measured directly because Be is transparent, but they are corroborated by the fact that the measured shock arrival time at the interface is 3.4 ns as calculated. The transmitted shock compresses the AGAR to a peak density $\rho_2^* \sim 0.5$ g/cm^3 and reaches the rear surface at ~ 9 ns. The calculated shock and interface velocities $V_2 \sim 46$ μm/ns and $U \sim 35$ μm/ns agree with the measured velocities within 10%. In Fig. 2(c), the calculated density profile (dashed) is compared to the measured optical depth profile (solid) at 6.5 ns. The optical depth is large in the shocked AGAR between the interface at $z \sim 225$ μm and the shock front $z \sim 255$ μm, but the maximum value $\tau \sim 3.5$ is limited by the instrumental resolution and dynamic range ($\Delta\tau < 5$). As a result of these limitations, we obtain an average compression by dividing the initial width of the AGAR (~ 275 μm) by its width at full compression (~ 75 μm) at 9 ns. This yields an average postshock density of $\rho_2^* \sim 0.42$ g/cm^3, which is 15% smaller than the peak calculated density, and a postshock Atwood number of $A^* = -0.68$.

The instability growth is measured with the face-on radiograph in Fig. 3(a) for the Be/AGAR target. Sinusoidal interfacial perturbations $z = \eta_0 \sin(kx)$ are imposed with $\lambda = 100$ μm and $\eta_0 = 14$ μm. The 1D image along x is displayed over 5 ns with an optical depth color scale. When the shock reaches the interface at 3.4 ns, a 180° phase reversal (characteristic for $A < 0$) occurs and the instability begins to grow. These features are quantified with optical depth profiles such as in Fig. 3(b) at 3.4 and 6.2 ns. The optical depth depends on the interface perturbation because the attenuation of the diagnostic x rays differs in Be and AGAR such that $\tau \sim \mathrm{MTF} \times (\rho_2^* \mu_2 - \rho_1^* \mu_1)\eta$. In fact, Be is chosen because its mass attenuation coefficient $\mu_1 = 30$ cm^2/g is small compared to $\mu_2 = 1050$ cm^2/g for doped AGAR at 2.6 keV. The instrumental modulation transfer function MTF ~ 0.67 at

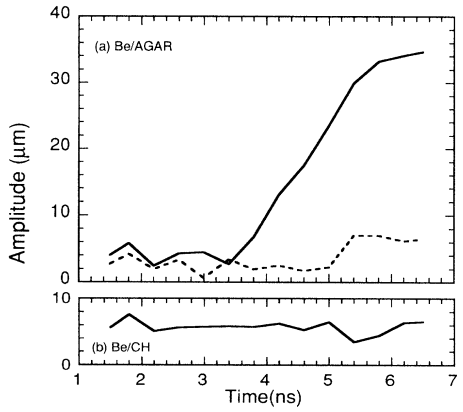

FIG. 4. (a) Amplitude of fundamental (solid) and harmonic (dashed) vs time for Be/AGAR target in Fig. 3. (b) Amplitude vs time for the Be/CH target. $\lambda = 100$ μm, $\eta_0 = 14$ μm in both.

$\lambda = 100$ μm is measured with grids [10] and undriven targets. We use the postshock densities $\rho_2^* \sim 0.42$ and $\rho_1^* \sim 2.2$ g/cm^3 to determine the opacity scale length $(\rho_2^* \mu_2 - \rho_1^* \mu_1)^{-1} \sim 27$ μm so that the amplitude units (μm) apply during the instability phase. The error in η is (10–15)% due to uncertainties in ρ_2^* and the MTF.

The optical depth profiles are Fourier analyzed to obtain the wave number spectrum. The temporal variation of the imposed mode ($\lambda = 100$ μm) and the harmonic are shown in Fig. 4(a) for the Be/AGAR target. The fundamental mode is constant until the shock reaches the interface at 3.4 ns and then grows at a constant rate $d\eta/dt \sim 13$ μm/ns until it saturates near 6 ns with $\eta_{\mathrm{sat}} \sim 35$ μm $\sim \lambda/3$. A bubble and spike may continue to grow nonlinearly as observed in [9], but at a reduced rate because the growth occurs in the higher harmonics.

Similar experiments and calculations are performed with the Be/CH target because the density contrast is smaller $A \sim -0.3$. The velocities $V_2 \sim 35$ μm/ns and $U \sim 26$ μm/ns are smaller in plastic because it is denser than AGAR, but the shock speed in the Be is similar. Here, the Be and plastic are compressed to similar densities $\rho_1^* \sim 4$ and $\rho_2^* \sim 3.6$ g/cm^3 which reduces the Atwood number to $A^* \sim -0.05$ and stabilizes the RM growth consistent with Fig. 4(b).

The saturation amplitude of the fundamental Fourier mode increases linearly with the wavelength as shown in Fig. 5 for the Be/AGAR targets. The instability may continue to grow late in time, but the growth occurs mainly in harmonics that produce the narrow spikes. In the RT instability, the acceleration is prolonged and a single mode saturates by reaching a terminal velocity when $\eta \sim \lambda/5$. In the RM instability, the acceleration is impulsive and the saturation is manifested one lower order in time with a terminal amplitude.

We now compare our results with linear theory. Since our targets have $A < 0$ for RT stability during the acceleration and Eq. (1) does not apply, we compare our

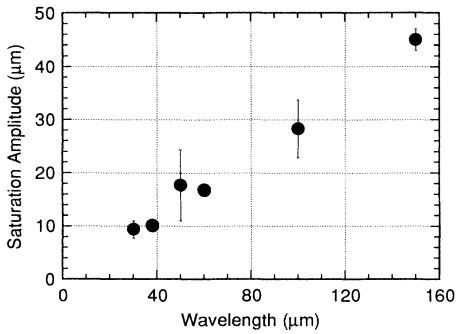

FIG. 5. Saturation amplitude vs wavelength.

measured growth rates with the empirical prescription of Meyer and Blewett [5],

$$d\eta/dt = A^* Uk\eta_0[(1-U/V_1)+1]/2 . \quad (2)$$

This resembles Eq. (1), but $(\eta_0+\eta_0^*)/2$ is used instead of η_0^*. For the Be/AGAR target ($A\sim -0.9$), the growth rate averaged over three shots is $d\eta/dt \sim 11 \pm 2$ μm/ns in agreement with Eq. (2) $d\eta/dt \sim 12$ μm/ns. As a result of the large compression $\eta_0^* = \eta_0(1-U/V_1) \sim \eta_0/8$, Eq. (1) yields a growth rate $A^* Uk\eta_0^* \sim 2.6$ μm/ns that is significantly smaller than measured. The failure of the Richtmyer formula, which was derived for $A > 0$, may be due to the strong reflected shock from the interface for $A < 0$ as described earlier. For the Be/CH target ($A\sim -0.3$), the measured growth rate is small, $d\eta/dt < 0.5$ μm/ns, in agreement with Eq. (2), $d\eta/dt \sim 0.8$ μm/ns. Thus, the postshock Atwood number $A^* \sim -0.05$ is important in determining the growth rate since $AUk\eta_0[(1-U/V_1)+1]/2 \sim 5$ μm/ns is larger than observed.

In conclusion, we have measured the linear growth and saturation of the shock induced Richtmyer-Meshkov instability under high compression using the Nova laser. The measured linear growth rates agree with the Meyer-Blewett prescription for $A < 0$, which specifies that the effective initial amplitude is the average of the pre- and postshock initial amplitudes. When the amplitude is large $\eta \sim \lambda/3$, the fundamental mode saturates and harmonics emerge marking the transition to a slowly developing bubble and spike.

We are indebted to R. J. Wallace, K. M. Weindorf, R. L. Morrison, T. G. Beat, J. Vargas from LLNL, and P. Slattery from Electrofusion, Inc., for target fabrication and to the Nova operations staff and D. Nelson for technical support. We thank P. Blewett for useful conversations, B. A. Hammel and R. A. Pasha for use of the streaked slit camera, and C. E. Frerking for help with LASNEX. We appreciate the continued support of M. J. Eckart and J. D. Kilkenny. This work was performed under the auspices of the U.S. Department of Energy by the Lawrence Livermore National Laboratory under Contract No. W-7405-ENG-48.

[1] R. D. Richtmyer, Commun. Pure Appl. Math. **13**, 297 (1960).
[2] E. E. Meshkov, Izv. Akad. Nauk SSSR Mekh. Zhidk. Gaza **4**, 151 (1969) [Izv. Acad. Sci. USSR Fluid Dynamics **4**, 101 (1969)].
[3] Lord Rayleigh, Scientific Papers II, 200, Cambridge, England, 1900; Sir Geoffrey Taylor, Proc. R. Soc. London A **201**, 192 (1950).
[4] H. Sakagami and K. Nishikara, Phys. Fluids B **2**, 2715 (1990).
[5] K. A. Meyer and P. J. Blewett, Phys. Fluids **15**, 753 (1972).
[6] L. D. Cloutman and M. F. Wehner, Phys. Fluids A **4**, 1821 (1992).
[7] R. F. Benjamin, D. C. Besnard, and J. F. Haas, Los Alamos Report No. LA-UR 92-1185 (unpublished).
[8] R. F. Benjamin and J. N. Fritz, Phys. Fluids **30**, 331 (1987).
[9] A. N. Aleshin *et al.*, Pis'ma Zh. Tekh. Fiz. **14**, 1063 (1988) [Sov. Tech. Phys. Lett. **14**, 466 (1988)].
[10] B. A. Remington *et al.*, Rev. Sci. Instrum. **63**, 5080 (1992).
[11] B. A. Remington *et al.*, Rev. Sci. Instrum. **63**, 5083 (1992); B. A. Hammel *et al.*, Report No. UCRL-JC-111933 [Phys. Fluids B (to be published)].
[12] B. A. Remington *et al.*, Phys. Rev. Lett. **67**, 3259 (1991); Phys. Fluids B **4**, 967 (1992).
[13] G. B. Zimmerman and W. L. Kruer, Comments Plasma Phys. Controlled Fusion **2**, 51 (1975).

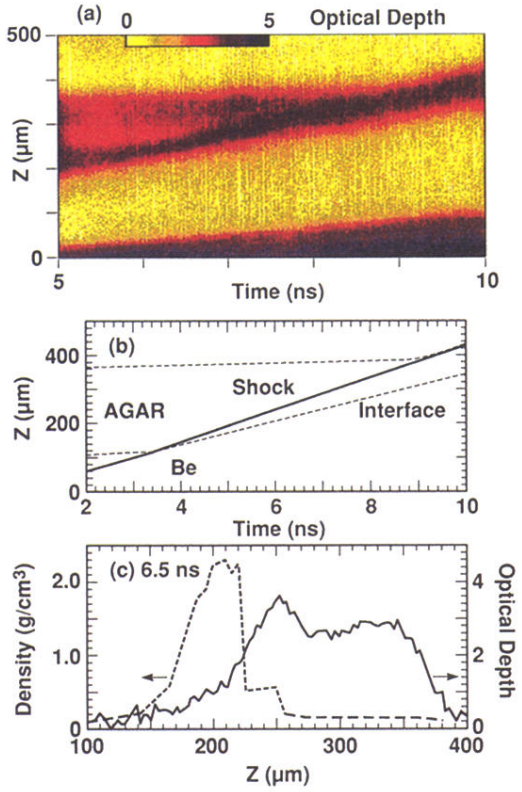

FIG. 2. (a) Transverse radiograph in optical depth of Be/AGAR target showing the shock characteristics. (b) Shock and interface trajectories from 1D LASNEX simulation. (c) Measured optical depth (solid) and calculated density (dashed) profiles at 6.5 ns.

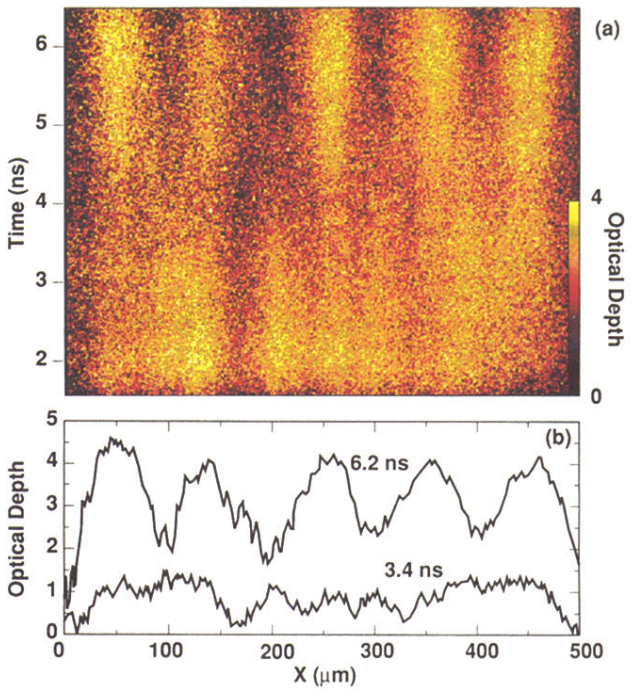

FIG. 3. (a) Face-on radiograph of Be/AGAR target showing instability growth. (b) Optical depth profiles averaged over 0.4 ns. Initial perturbations have $\lambda = 100\ \mu$m, $\eta_0 = 14\ \mu$m.